Characterization of granite matrix porosity and pore-space geometry by *in situ* and laboratory methods

M. Schild,[1] S. Siegesmund,[1,2] A. Vollbrecht[1] and M. Mazurek[3]

[1] *Institut für Geologie und Dynamik der Lithosphäre,* 37077 *Göttingen, Goldschmidtstrasse* 03, *Germany. E-mail: ssieges@gwdg.de*
[2] *Geol.-Paläont. Institut, Bernoullistrasse* 32, 4056 *Basel, Switzerland*
[3] *GGWW, Institutes of Geology and of Mineralogy and Petrology, University of Bern, Baltzer-Strasse* 1, 3012 *Bern, Switzerland*

SUMMARY

Most available studies of interconnected matrix porosity of crystalline rocks are based on laboratory investigations; that is, work on samples that have undergone stress relaxation and were affected by drilling and sample preparation. The extrapolation of the results to *in situ* conditions is therefore associated with considerable uncertainty, and this was the motivation to conduct the '*in situ* Connected Porosity' experiment at the Grimsel Test Site (Central Swiss Alps). An acrylic resin doped with fluorescent agents was used to impregnate the microporous granitic matrix *in situ* around an injection borehole, and samples were obtained by overcoring. The 3-D structure of the pore-space, represented by microcracks, was studied by U-stage fluorescence microscopy. Petrophysical methods, including the determination of porosity, permeability and *P*-wave velocity, were also applied. Investigations were conducted both on samples that were impregnated *in situ* and on non-impregnated samples, so that natural features could be distinguished from artefacts.

The investigated deformed granites display complex microcrack populations representing a polyphase deformation at varying conditions. The crack population is dominated by open cleavage cracks in mica and grain boundary cracks. The porosity of non-impregnated samples lies slightly above 1 per cent, which is 2–2.5 times higher than the *in situ* porosity obtained for impregnated samples. Measurements of seismic velocities (V_p) on spherical rock samples as a function of confining pressure, spatial direction and water saturation for both non-impregnated and impregnated samples provide further constraints on the distinction between natural and induced crack types. The main conclusions are that (1) an interconnected network of microcracks exists in the whole granitic matrix, irrespective of the distance to ductile and brittle shear zones, and (2) conventional laboratory methods overestimate the matrix porosity.

Calculations of contaminant transport through fractured media often rely on matrix diffusion as a retardation mechanism.

Key words: contaminant transport, fractured media, Grimsel Test Site, permeability, porosity, seismic anisotropy.

INTRODUCTION

Matrix porosities of crystalline rocks are mostly below 1 per cent and are attributed to open intra- and intergranular microcracks. These are common features of rocks that have undergone deformation, and commonly they display complex composite systems which have formed progressively by a variety of geological processes and under varying conditions over long time spans. In granitic rocks, natural microcracking can be related to thermal contraction during cooling, tectonic stresses during stages of deformation, and stress relaxation during uplift and unroofing (Kowallis & Wang 1983). The lifetime of natural microcracks depends on the geological environment; that is, on the percolation of fluids which may cause healing or sealing of interconnected cracks

Open (*in situ*) cracks may be of special interest for the following reasons:

(1) further propagation and coalescence of open cracks at different stress states finally leads to macroscopic fractures, and hence control the mechanical behaviour in the brittle regime (e.g. Hallbauer *et al.* 1973);

(2) interconnected, open cracks yield pathways for fluid flow and solute diffusion (e.g. France-Lanord *et al.* 1988);

(3) if open cracks display preferred orientations they may also contribute significantly to the anisotropy of petrophysical and mechanical properties (e.g. Anderson *et al.* 1974; Peng & Johnson 1972); and

(4) the orientation of open microcracks can often be used as an indicator of the recent to subrecent stress directions (e.g. Vollbrecht *et al.* 1994).

The characterization of the microporous matrix is also relevant for some practical applications, including exploitation of thermal energy (e.g. Hot Dry Rock technology) and the quantification of contaminant transport through geological formations (e.g. Mazurek 2000). Porosity and permeability are among the most important parameters for energy and mass transport through rocks. Thus the frequency and geometry of cracks and pores on all scales, and their type and degree of saturation are relevant characteristics of these reservoir rocks. Several countries (including France, Canada, Sweden, Finland and Switzerland) consider crystalline rocks as hosts for radioactive and industrial waste. Most disposal concepts take advantage of the barrier function of the host rock for flow and transport. The potential of a fractured rock system to retard contaminant migration is greatly increased if the rock matrix adjacent to fractures contains an interconnected network of micropores that is accessible to diffusion (e.g. Neretnieks 1980). Diffusion into the matrix not only dilutes contaminant concentrations in fractures where advection occurs but also provides access to mineral surfaces in the matrix on which contaminants can be sorbed. The combined action of matrix diffusion and sorption on matrix minerals is efficient in retarding contaminant exfiltration and in reducing peak concentrations.

In their classical experimental study, Norton & Knapp (1977) calculated diffusion-accessible porosities on the basis of measured KCl breakthrough curves. These porosities were small compared to the total porosity, leading to the conclusion that a large part of the microscopic pore space of the investigated samples is not connected ('residual porosity'). However, a wealth of more recent studies (e.g. Hellmuth *et al.* 1995; Siitari-Kauppi *et al.* 1998) indicate that the diffusion-accessible porosity is substantially larger than the one measured by Norton & Knapp (1977), and dominates quantitatively over residual, i.e. unconnected, porosity. Rasilainen *et al.* (1996) compared a large number of laboratory-based analytical techniques to measure the porosity of crystalline rocks. The results were encouraging in that all methods provided consistent results.

However, all of these measurements were performed in the laboratory, and it is still unclear how they can be extrapolated to *in situ* conditions. The quantification of analytical artefacts is one of the major difficulties in characterizing low-porosity rocks. A number of processes may affect porosity measurements in the laboratory, including the following (see Fig. 1):

(1) the generation of microcracks during drilling (due to Kirsch and bottom-hole stresses and due to the mechanical impact of drilling);

(2) the stress release from lithostatic to atmospheric pressure; and

(3) the generation of microcracks during sample preparation (cutting, drying).

In porous rocks, such as shales or sandstones, these effects will be small compared with the *in situ* porosity of the rocks. In contrast, they may be substantial in low-porosity rocks, such as fresh crystalline rocks. In addition, the connectivity of the microcrack network may also be affected, such that laboratory measurements of permeability and diffusivity may not be representative of *in situ* conditions.

THE 'CONNECTED POROSITY' EXPERIMENT

The main motivation to conduct the Connected Porosity experiment (Frieg *et al.* 1998) was to reduce and quantify analytical artefacts inherent in all laboratory methods and thereby obtain matrix porosities that more closely represent *in situ* values. Further objectives included the characterization of the pore-space geometry and pore connectivity. This field experiment was performed by Nagra (Swiss National Cooperative for the Disposal of Radioactive Waste) at the Grimsel Test Site (GTS), located in the Central Swiss Alps at a depth of about 400 m below surface.

The basic principle of the Connected Porosity experiment included the *in situ* injection of a low-viscosity, fluorescene-doped resin into the rock matrix under near-natural stress conditions from a set of borehole intervals, subsequent polymerization of the resin by a heat pulse, and overcoring of the whole experimental array. Over the time of the injection period, the penetration depth of the resin into the surrounding matrix was of the order of 5 cm (Möri *et al.* 1996, 1999). Resin-filled pore spaces can be observed and quantified in slices and thin sections of the overcore under UV light and compared with non-impregnated samples from the same locality. Samples from the Connected Porosity experiment are the basis for this paper, and the field information is evaluated and augmented by ancillary laboratory studies. The samples examined in this paper (LS, SZ, HS) were chosen along a profile across a shear zone in the Grimsel granodiorite (see Fig. 2). This shear zone consists of a fine-grained, mica-rich mylonite about 10 cm thick, which was reactivated as a brittle, gouge-bearing fault during regional uplift (Steck 1968). Samples were chosen such that porosity could be monitored as a function of the distance to the shear zone.

By its design, the Connected Porosity experiment fully eliminates artefacts created during sample preparation, and greatly reduces the effects of stress release (points 2 and 3 above). The possible generation of microcracks during drilling (point 1 above) cannot be fully avoided because resin impregnation of the rock matrix did not much exceed 1 diameter of the injection borehole.

GEOLOGICAL SETTING

The Grimsel Test Site (GTS) is situated in the Aar Massif, a basement high in the Helvetic realm of the Alps. The Aar Massif consists of a metasedimentary envelope that was intruded by Hercynian granitoids (320–280 Ma) such as the Central Aare granite and the Grimsel granodiorite; the latter is the host rock of the site investigated. All rocks of the Aar Massif have been affected by Alpine greenschist metamorphism and deformation at about 25 Ma (Dempster 1986). The plutonic rocks were transformed to gneisses. Structures in the Hercynian plutonic rocks are mostly attributed to Alpine deformation (Steck 1968; Marquer & Gapais 1985).
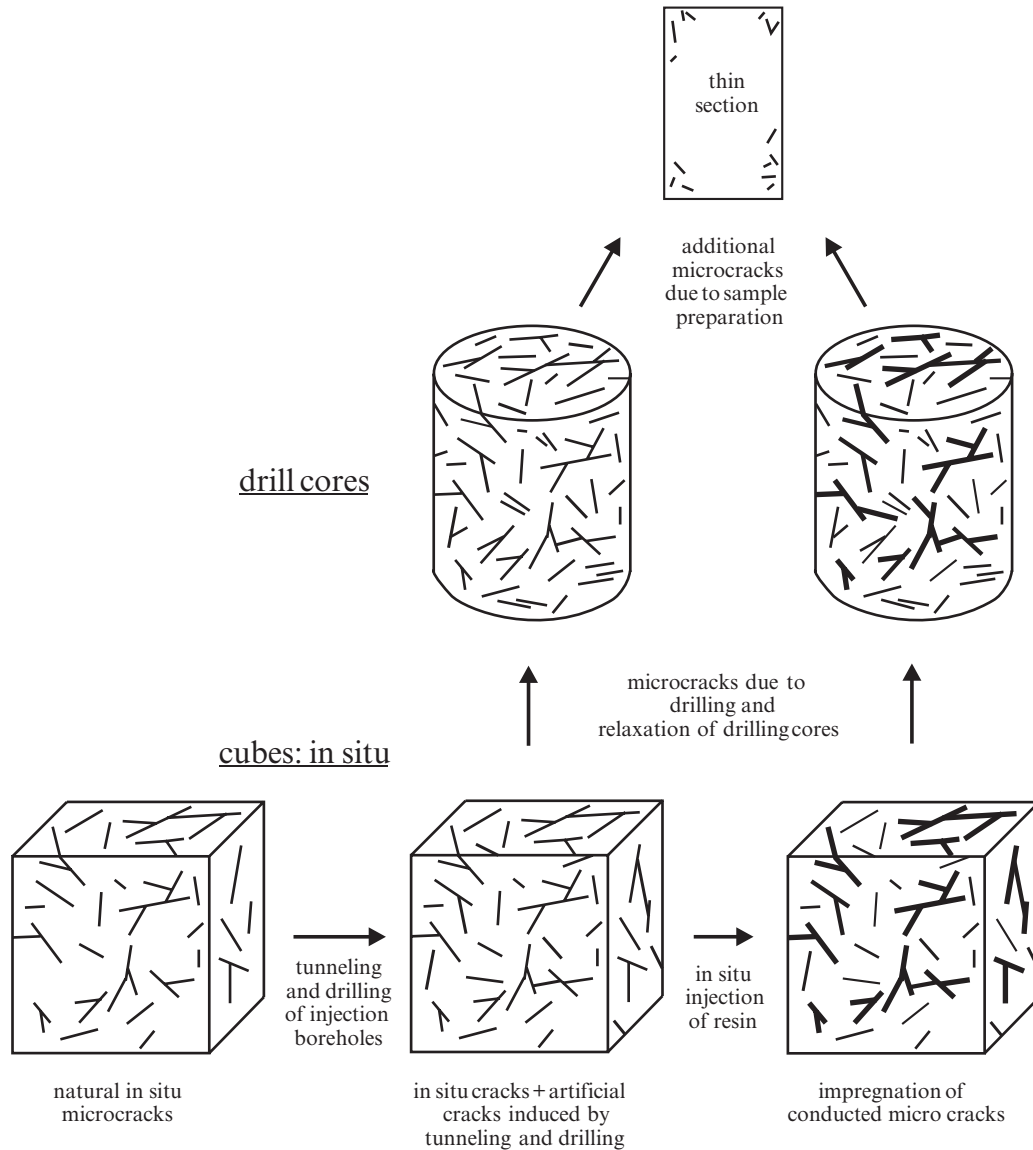
Figure 1. Schematic diagram of the influence of tunnelling, injection and sample relaxation after drilling of the impregnated and non-impregnated samples. Thin lines: open microcracks; thick lines: impregnated microcracks. For further explanation see text.

Peak Alpine metamorphic conditions in the vicinity of the GTS are estimated at 400 °C/2.5–3 kbar (Choukroune & Gapais 1983; Marquer *et al.* 1985). The following structural elements can be assigned to this greenschist facies metamorphism and associated ductile deformation: cleavage, mylonitization (including formation of quartz ribbons), mineral stretching lineation, extension fractures and quartz recrystallization. Within this ductile matrix feldspars and allanite (=orthite) show a brittle deformational behaviour.

The formation of brittle structures, which are common in the crystalline rocks at Grimsel, post-dates the ductile deformation and can be attributed to the post-metamorphic regional uplift that is still operative at present with rates of 1–2 mm yr^{-1}. In most cases, faults run along pre-existing mylonitic zones and are parallel to metamorphic cleavage (see inset in Fig. 2). The brittle structural elements include both cataclastic fault breccias and discrete fractures. Brittle deformation occurred at significantly lower temperatures and pressures than the preceding ductile deformation.

TECHNICAL AND EXPERIMENTAL CONCEPTS

In situ impregnation

In order to inject the water-saturated microporosity of the rock matrix, specific properties of the injection resins are required. These include mainly good wetting properties, good miscibility with the *in situ* pore-water, limited reactivity with pore-water, and low viscosity. Moreover, the resin needs to remain liquid for the duration of the experiment (weeks to months) and polymerize only after heating. A new acrylic resin was developed for the purpose of the Connected Porosity experiment and is described in Frieg *et al.* (1998). The experimental procedure included the following steps (details in Möri *et al.* 1999; see also Fig. 2).

(1) Drilling of four boreholes (diameter 40 mm) for resin injection into the rock matrix adjacent to a fault.
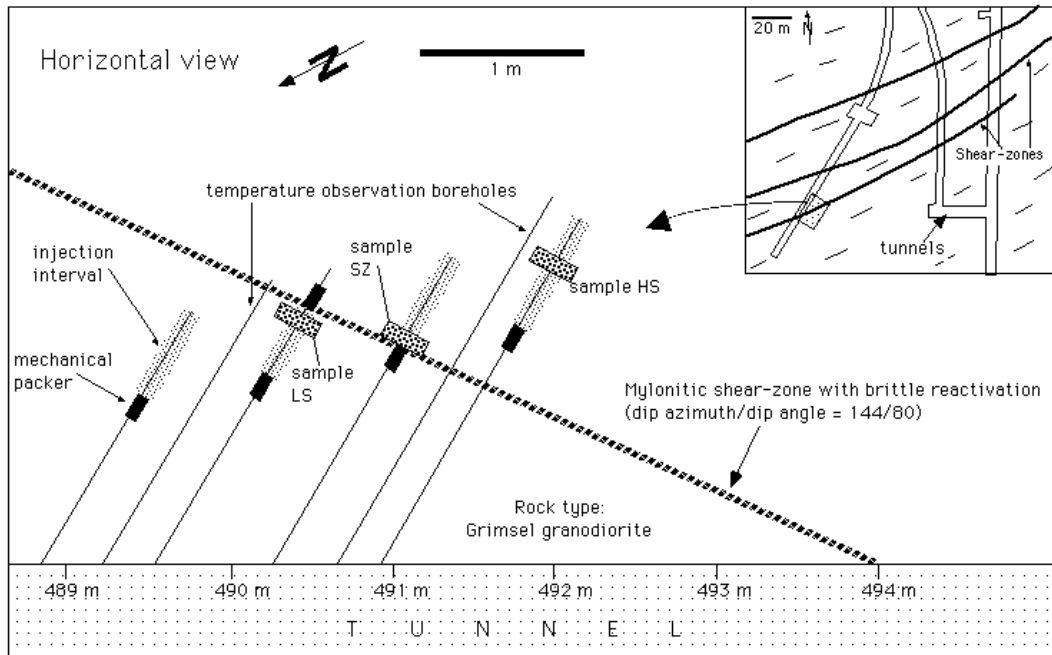
Figure 2. Overview of the set-up of the Connected Porosity experiment at the Grimsel Test Site (adapted from Möri *et al.* 1999).

(2) Drilling of two boreholes (diameter 16 mm) for temperature observation.

(3) Installation of a packer system in the injection boreholes, and injection of acrylic resin into the rock (20 bar overpressure for about 1 month).

(4) Removal of packer and resin from the boreholes, installation of a heating element, and heating (80 °C) for about 8 weeks to polymerize the resin. Temperature sensors were installed at distances of 20–30 cm from the injection boreholes to check whether the temperature exceeded 40 °C (the temperature required for resin polymerization).

(5) Overcoring of the boreholes (core diameter 200 mm).

Sample reference system

All samples (thin sections, cylinders and spheres) were orientated with respect to the macroscopic fabric elements (foliation, lineation) as shown in Fig. 3. As for all other fabric diagrams, the pole figures were plotted on a Schmidt net (lower hemisphere) with x orientated parallel to the lineation; the xy-plane is the foliation plane, and z is coaxial with the foliation pole.

U-stage fluorescence microscopy

The 3-D patterns of microcracks (orientations and frequencies of different types) were measured on standard thin sections using a fluorescence microscope equipped with a Universal-stage (U-stage). In order to record all microcrack orientations, the measurements for each sample were carried out in three mutually perpendicular sections. There is no evidence that a significant number of open cracks were produced during sample preparation, since the cracks show a consistent orientation in different thin sections. Moreover, the orientation and geometry of the microcracks are independent of the sample geometry.

Composite pole figures were computed from the three sections, and errors induced by the overlap of Schmidt net areas were statistically eliminated (for details see Vollbrecht *et al.* 1991).
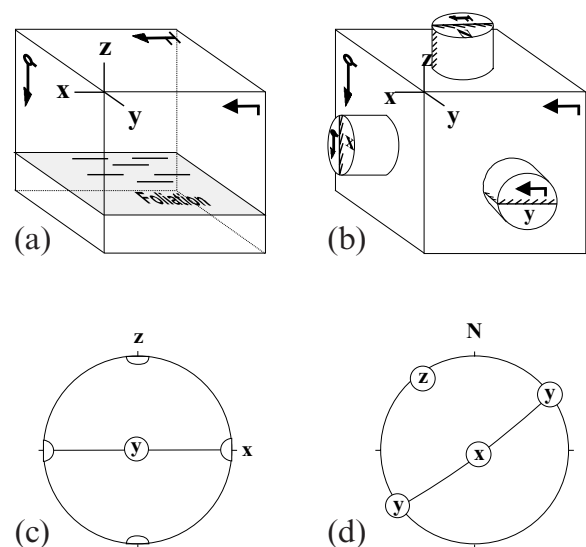

Figure 3. Reference system of the sample orientation. (a) Schematic cube with foliation (xy-plane) and lineation (x-direction); the arrows indicate the orientation of the thin sections. (b) Orientation of cylindrical samples for the permeability measurements. (c) Projection of the foliation and lineation of the sample cube and (d) coordinates with respect to the geographic reference system in the Schmidt net, lower hemisphere.

During U-stage measurements the microcracks were classified according to their host grain, position (inter- or intragranular, interphase), and state (open, healed, sealed; Schild 1999). For this particular study, however, only open cracks impregnated *in situ* with acrylic resin and non-impregnated open cracks were considered, in order to discriminate *in situ* crack porosity from cracks formed during core relaxation and sample preparation. The microcrack fabrics were also quantified indirectly by using petrophysical methods (see below).

Porosity and hydraulic conductivity

Porosity was determined by buoyancy weighting at room temperature. For the investigation of permeability, three orthogonal cylindrical specimens were drilled along the directions of the macroscopic fabric elements (see Fig. 3). The measurements were performed up to a confining pressure of 20 MPa. A pressure transient method using argon gas as a flow medium was used. The gas pressure at the front of the sample was kept constant at 5 MPa. The pressure increase at the back of the samples, measured in a constant volume as a function of time, was used to calculate the permeability (for details see Nover *et al.* 1995). The permeability was then recalculated to hydraulic conductivity.

Seismic velocities

An experimental determination of the compressional-wave velocities (V_P) was performed to quantify the observed microcrack patterns indirectly. The wave velocity measurements (V_P) were carried out on spherical samples (diameter = 50 mm ± 0.01 mm) under dry and water-saturated conditions at atmospheric pressure. In addition, the complete patterns of V_P were determined at confining pressures of up to 100 MPa (see Siegesmund *et al.* 1993). The samples were covered by an epoxy resin film to protect them against the pressure medium.

The measuring system in which the samples were mounted allows a rotation of 360° on the vertical axes and 75° around the horizontal axes. Within this system it is possible to measure the P-wave velocity in any direction with the same accuracy. Usually, 132 independent measuring directions were analysed. The P waves were generated and measured by piezoceramic transducers with a 2 MHz resonance frequency. Three different approaches were introduced: (1) velocity measurements at selected confining pressure levels; (2) V_P at atmospheric pressure under dry and saturated (sat) conditions; and (3) analyses of the V_P pattern for comparable impregnated and non-impregnated rock samples.

RESULTS

Petrography and microstructure

All investigated samples show a comparable mineralogical composition. They are mainly composed of K-feldspar (12–24 vol. per cent), plagioclase (29–30 vol. per cent), quartz (27–28 vol. per cent) and biotite (7–11 vol. per cent), with accessory muscovite/sericite, apatite, sphene, epidote, zircon, chlorite, calcite and opaques.

The foliation which is developed in all samples (see Fig. 4) is defined by compositional banding of alternating dark biotite layers and quartz-rich layers. The macroscopically visible lineation is represented by aggregates (rods) of K-feldspar and plagioclase. The K-feldspar, mainly microcline, exhibits rare twinning after the Karlsbad law, and shows different features of alteration and brittle deformation. The fractures are often filled with feldspars and recrystallized quartz. Diffuse perthitic exsolution lamellae are visible by different degrees of sericitization. Oligoclase, twinned after the albite law, is also intensely sericitized. The grain size of K-feldspar varies between 100 μm and 1–2 cm, while that of plagioclase is smaller. Quartz occurs

as aggregates of equigranular grains, and it is evident from relic structures that they originated by rotation recrystallization. The size of these equigranular quartz grains generally ranges between 100 and 200 μm. Larger grains (up to 1 cm) show undulatory extinction and subgrain boundaries.

The grain size of the mostly recrystallized biotite is approximately equal to that of quartz, while that of secondary muscovite/sericite is smaller. Sometimes the biotite is altered to chlorite, especially along cleavage cracks. The mica (001)-cleavage planes are orientated parallel to the foliation, whereas deviating orientations result from reorientation along phase boundaries (mainly K-feldspar and plagioclase). All samples show a great variation in grain size. The feldspars in particular show extensive features of brittle deformation. The microfractures within larger feldspars are often orientated normal to the lineation.

During greenschist-stage regional metamorphism and deformation, both feldspars behave in a brittle manner and occur as porphyroclasts. Quartz, on the other hand, is largely recrystallized into mosaic-type ribbons and is deformed in a ductile style. The shear-zone sample SZ is a mylonite without macroscopic brittle discontinuities. It has a fine-grained, strongly recrystallized fabric.

Microcrack fabrics

Resin-impregnated pore spaces are related to an interconnected network composed of various crack types, as evident from fluorescence microscopy (Fig. 5). Most frequent are mica cleavage cracks (Figs 5a and b), intergranular cracks within quartz polycrystals (Figs 5c and d), and intragranular cracks in feldspars formed along cleavage planes (Figs 5e to h). More irregularly formed cracks in feldspars probably formed not parallel to crystallographic planes (Figs 5g and h). In addition, few interphase cracks between quartz and feldspars have been detected. The majority of cracks that were not resin-impregnated (and therefore represent artefacts) include a second set of mica cleavage cracks.

With only a few exceptions, the microcracks in mica (biotite and white mica) developed parallel to the (001)-cleavage planes, and a distinction between open and non-impregnated and impregnated cracks is only possible by fluorescence microscopy at high magnification. Mineralizations were not observed within cleavage cracks. Because alteration phenomena or coatings along open non-impregnated cleavage cracks are lacking, it is assumed that they formed mostly during core relaxation or sample preparation. However, it cannot be excluded that individual open cleavage cracks formed earlier but were isolated from the interconnected network. The corresponding crack pole figures are directly correlated with the mica textures and show comparable patterns for the three samples; that is, a concentration close to the foliation normal (*z*) and a tendency to form a girdle around the lineation (*x*; Figs 6a to c). The sample from the ductile shear zone (SZ) shows the strongest preferred orientation, which corresponds to the distinct mylonitic foliation and the related mica textures. The scattering of crack poles from the *z*- to the *x*-direction may be explained by lens-shaped feldspar porphyroclasts which control the shape orientation of the mica flakes. Accordingly, for sample SZ the stronger concentration of crack poles around *z* can be related to increasing mylonitization, which causes a flattening and grain size reduction of the porphyroclasts.
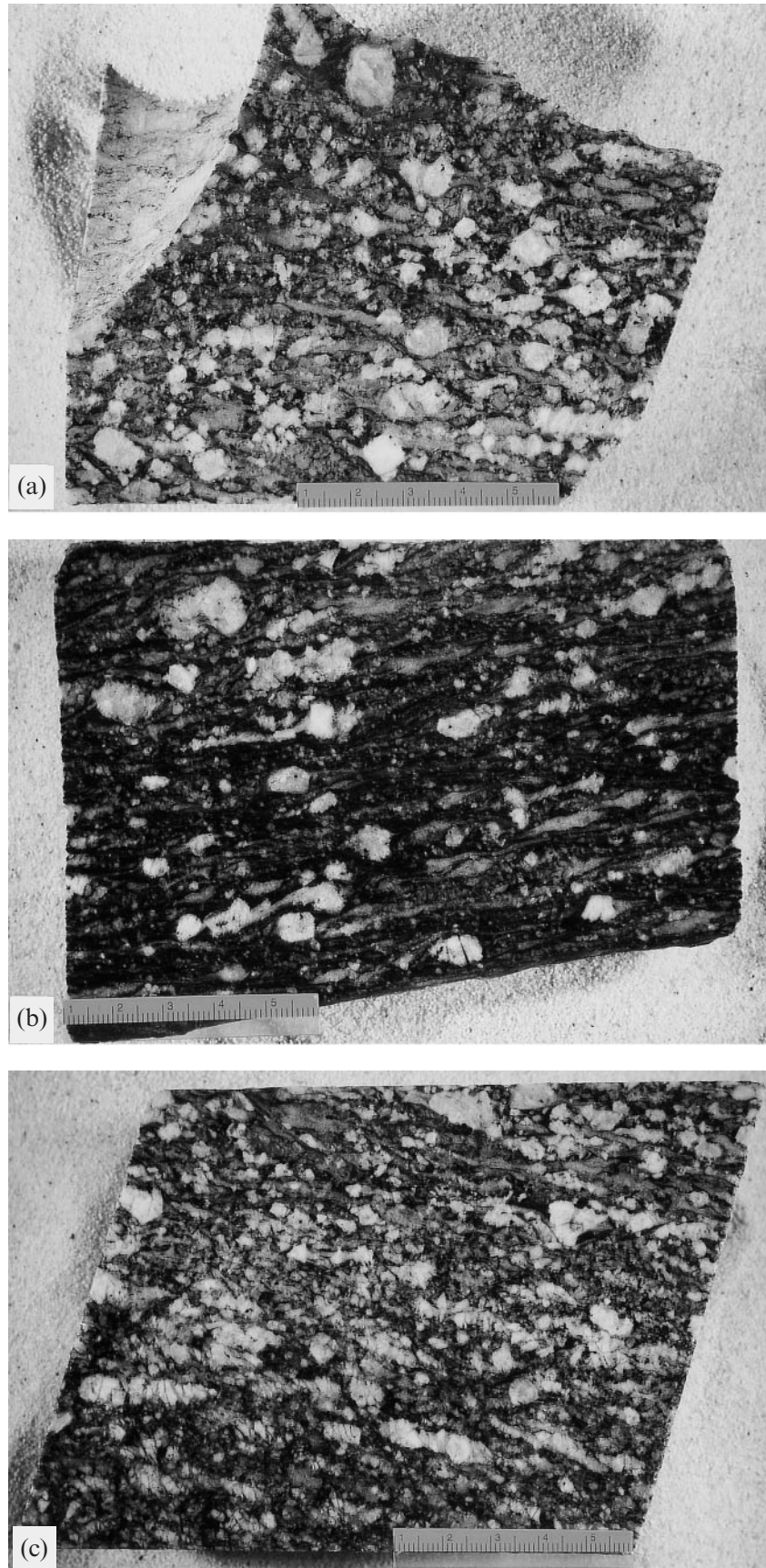
Figure 4. Rock fabric of the samples (a) HS, (b) SZ and (c) LS; lineation strikes parallel to the longer edge. The foliation is visible from the parallel alignment of mica flakes and elongated quartz ribbons and feldspars. Especially in LS the cataclase of feldspars is obvious; the white feldspar is crossed by grey minerals of quartz.
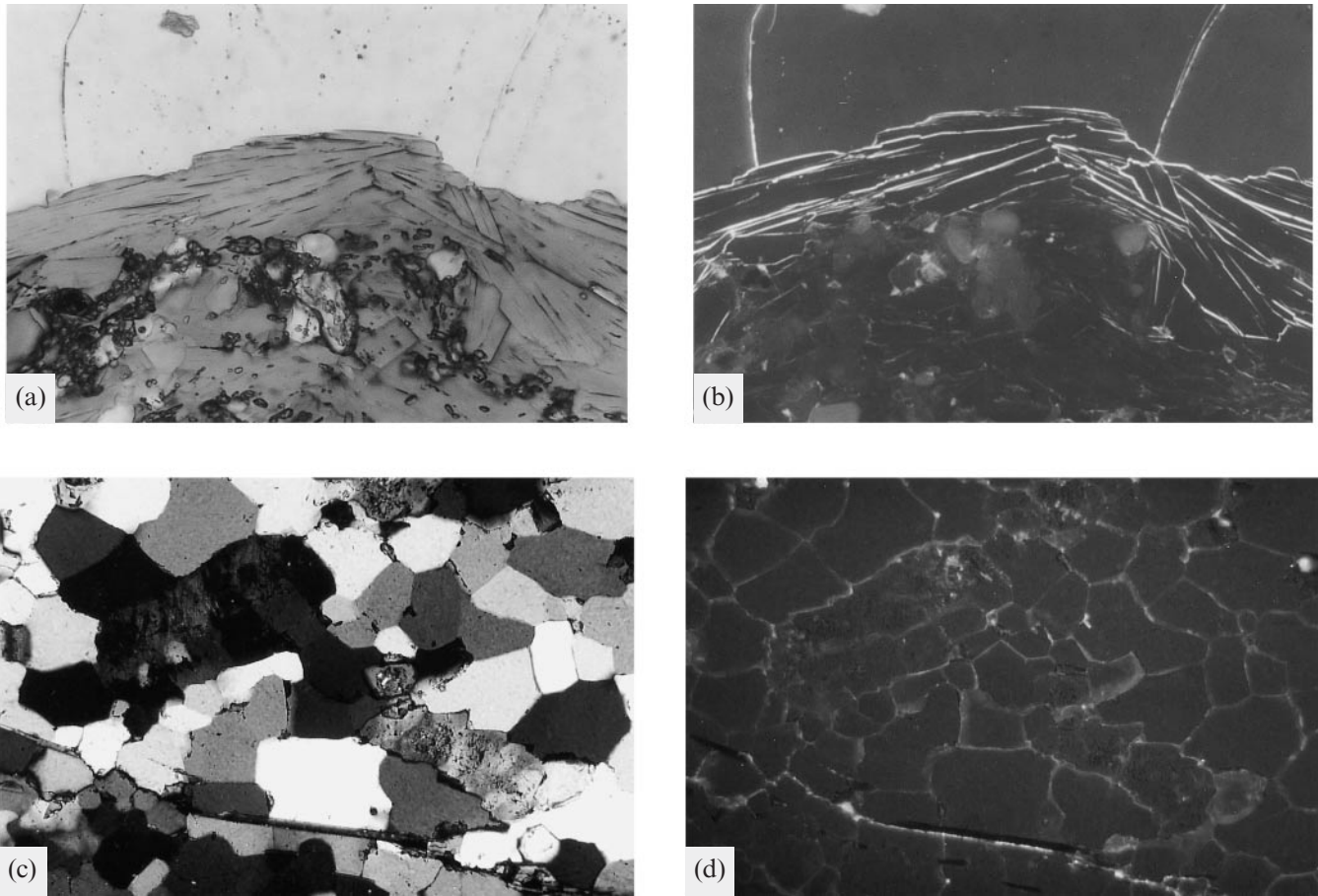
Figure 5. Thin sections of the impregnated samples: (a), (b), (c) and (g) normal, and (b), (d), (f) and (h) fluorescence microscopy. Characteristic microcracks are shown as follows: (a) and (b) (001)-cleavage cracks of biotite; some of the intergranular cracks are connected with microcracks in quartz; *yz*-plane; sample SZ; short edge: 0.28 mm. (c) and (d) Intergranular cracks in quartz polycrystals forming a well-developed inter-connected network; *xz*-plane, lineation parallel to the long edge; sample HS. (e) and (f) cleavage cracks of K-feldspars; the two cleavage cracks form a regular network; *xy*-plane, lineation parallel to the short edge; sample HS. (g) and (h) Irregular intragranular and intergranular cracks of plagioclase which are connected with intergranular cracks of quartz polycrystals; *xz*-plane, lineation parallel to the long edge; sample LS; short edge: 1.33 mm.

The intergranular cracks in quartz polycrystals form a well-developed interconnected network which is almost completely impregnated, indicating that they existed *in situ*. Their lengths range approximately between 100 and 200 μm. Scanning electron microscopy reveals that these cracks display rather rough surfaces. In contrast, non-impregnated open intergranular cracks in quartz are comparatively rare, and show a maximum length of only 100 μm and smaller widths. In addition, few intragranular open cracks were observed. The crack pole figures for open interconnected *in situ* cracks (Figs 6g to i), which are controlled by the prevailing intergranular network, show for all three samples an orthogonal pattern with a weak tendency of girdles around the reference axes (*x*, *y*, *z*).

The population of impregnated *in situ* cracks in K-feldspar comprises one or two sets of cleavage cracks and, in addition, irregularly shaped cracks often forming an anastomosing network which usually cuts the cleavage cracks at high angles. The widths of these irregular cracks vary from section to section. For cleavage cracks, it is apparent that *in situ* opening and impregnation preferentially occurred on cracks that are inclined at a high angle to the foliation (*xy*-plane). In a few cases, impregnated cracks were observed along K-feldspar phase boundaries, too. The lengths of both cleavage cracks and irregular cracks vary considerably up to about some 100 μm,

while the length of phase boundary cracks is strongly dependent on the grain size. In contrast, non-impregnated open cracks in K-feldspar are rare and are mostly represented by isolated intragranular cracks which often lack any connection with grain or phase boundaries (as indicated by 2-D observation in thin sections).

The impregnated *in situ* cracks in plagioclase display the same features as those in K-feldspar. In plagioclase, intragranular cracks are less frequent, while grain or phase boundary cracks are more frequent than in K-feldspar. The intragranular cracks are dominated by the irregular type described above. In contact zones between plagioclase and quartz polycrystals, the grain boundary cracks of both phases form a common interconnected network. Plagioclase grain boundaries are often decorated by mica flakes that also contain minute intragranular cracks which are connected with this network. As observed for K-feldspar, plagioclase also displays only a few non-impregnated open cracks. Most of them are very small isolated intragranular cracks with irregular curved shapes. Only a few non-impregnated open cracks parallel to twin lamellae have been observed.

Considering impregnated *in situ* cracks in K-feldspar and plagioclase together, the composite crack pole figures display orthogonal patterns which are comparable with those described for cracks in quartz (Figs 6d to f).
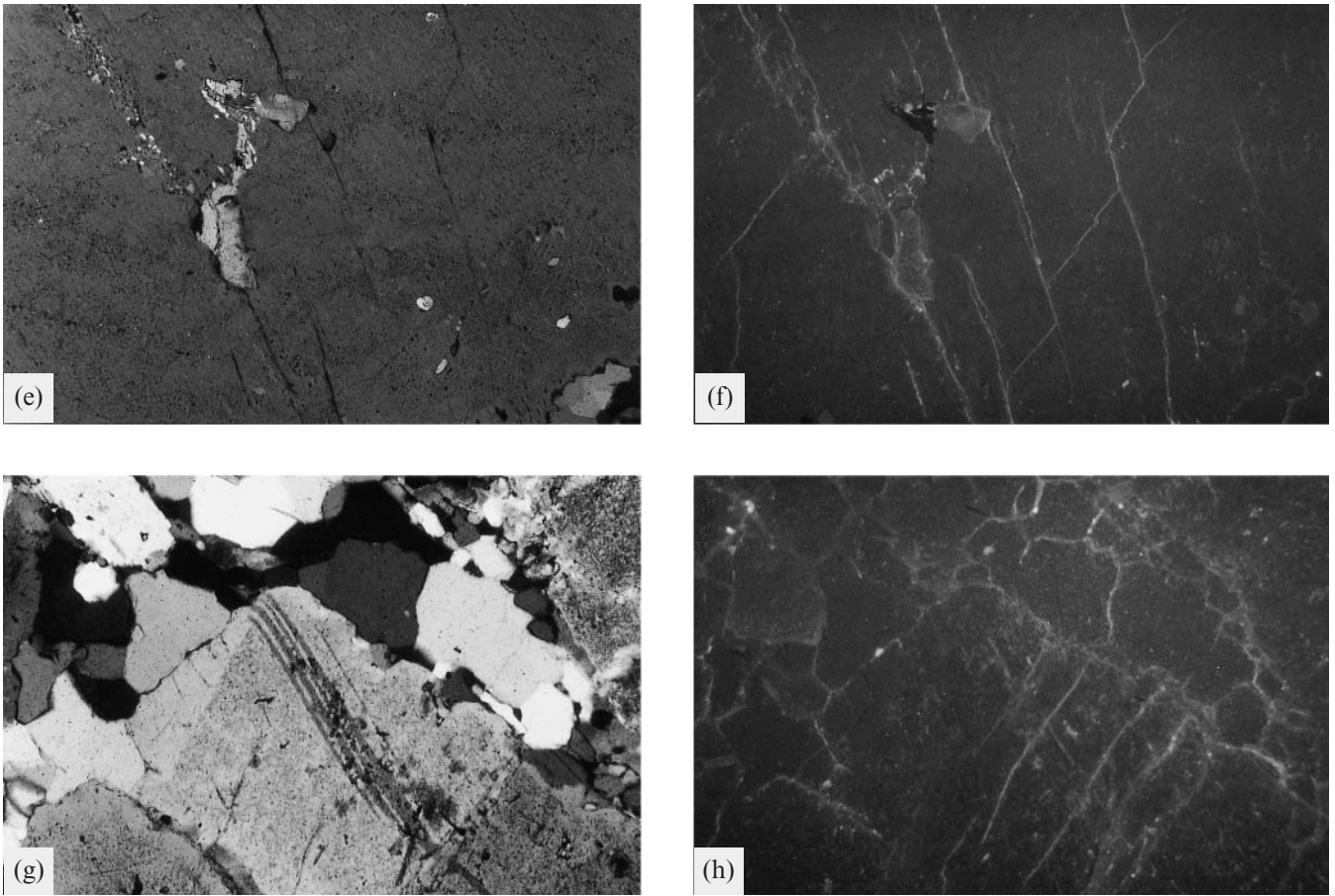
(e)

(f)

(g)

(h)

Figure 5. (*Continued.*)

Porosity and hydraulic conductivity

The results of the porosity measurements are given in Fig. 7. As is known, the porosity is very low in crystalline rocks and covers the range between 1 and 1.17 per cent. Most of the porosity is found as crack porosity. The impregnated samples clearly show a distinctly lower porosity, between 0.55 and 0.59 per cent.

The pressure dependence of the permeability/hydraulic conductivity is shown in Fig. 8 and Table 1. The permeability decreases by 50 per cent for HS_{impx} and 1/3 for HS_{nix} (where the subscript imp denotes impregnated and the subscript ni denotes non-impregnated) from 5 to 20 MPa (Fig. 8). The anisotropy of the permeability is obvious. Typically, the permeability is low normal to the foliation plane (z-direction), while larger

Table 1. Pressure-dependent permeability (μD) and hydraulic conductivity (m s^{-1}) of impregnated (imp) and non-impregnated (ni) samples in the direction parallel to the lineation (x) and perpendicular to the foliation (z).

|	Permeability (μD)	Conductivity (m s^{-1})	Permeability (μD)	Conductivity (m s^{-1})
Pressure (MPa)	5	5	20	20
HS_{impx}	1.0506	7.89E$-$12	0.3841	2.89E$-$12
HS_{impz}	0.1189	8.93E$-$13	0.0355	2.67E$-$13
HS_{nix}	2.5241	1.90E$-$11	0.6513	4.89E$-$12
HS_{niz}	0.8947	6.72E$-$12	0.2247	1.69E$-$12
Pressure (MPa)	2.5	2.5	20	20
SZ_{impx}	0.7654	5.75E$-$12	0.2152	1.62E$-$12
SZ_{impz}	0.1743	1.31E$-$12	0.057	4.28E$-$13
SZ_{nix}	0.5783	4.35E$-$12	0.1522	1.14E$-$12
SZ_{niz}	0.3487	2.62E$-$12	0.0948	7.12E$-$13
Pressure (MPa)	5	5	20	20
LS_{impx}	0.7998	6.01E$-$12	0.2046	1.54E$-$12
LS_{impz}	0.213	1.60E$-$12	0.0602	4.52E$-$13
LS_{nix}	0.5129	3.85E$-$12	0.0753	5.66E$-$13
LS_{niz}	0.433	3.25E$-$12	0.1334	1.00E$-$12

HS SZ LS
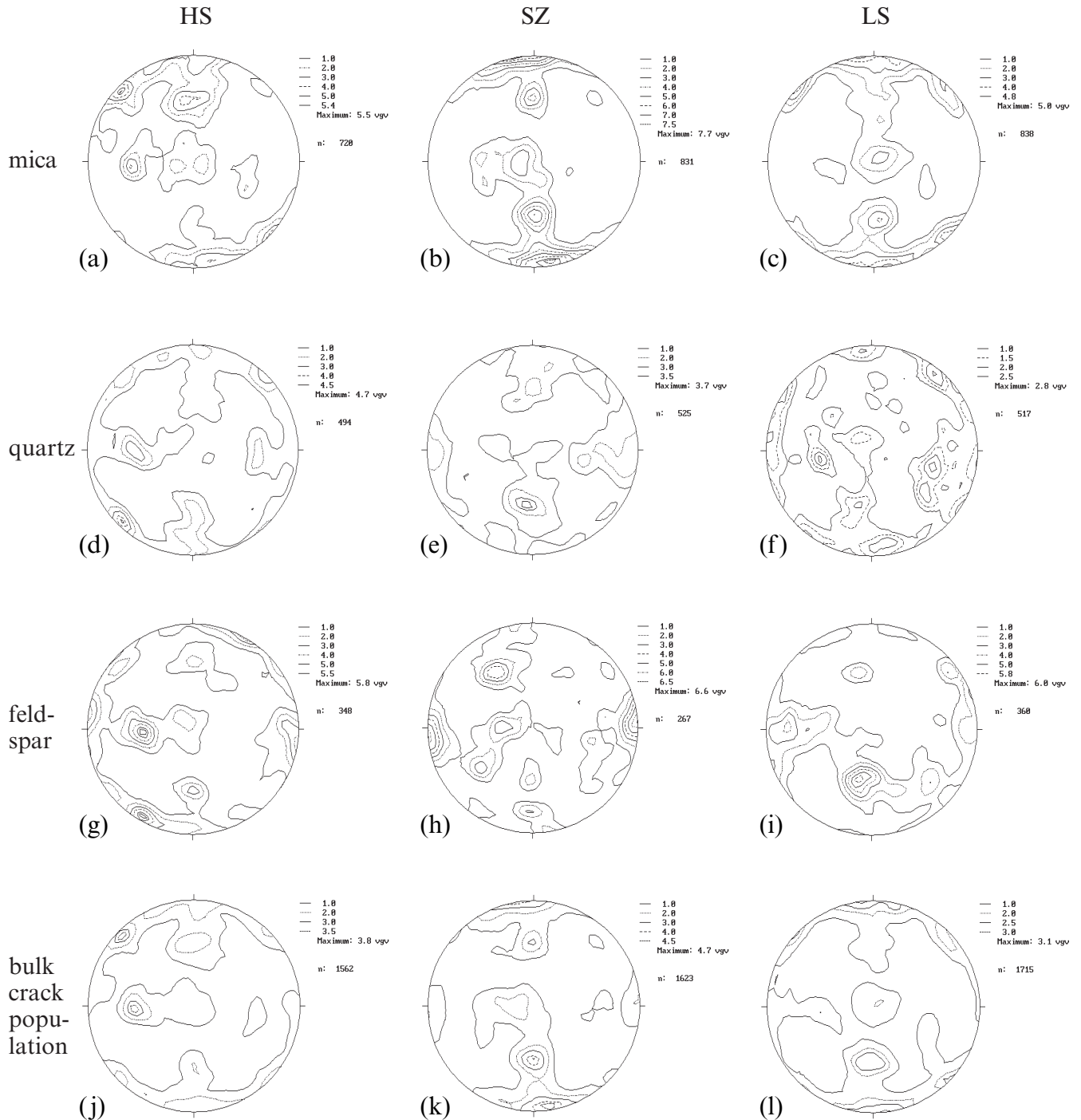
Figure 6. Pole figures of microcracks for the samples HS, SZ and LS: (a) to (c) (001)-cleavage planes of micas; (d) to (f) microcracks in quartz; (g) to (i) microcracks in feldspars; and (j) to (l) bulk crack fabric; Schmidt net, lower hemisphere; n = number of measured cracks, and vgv = multiple of random distribution

values are detected at higher pressures within the foliation plane, thus indicating that cracks remain open up to pressures of 20 MPa (Table 1).

Comparison of the permeability/hydraulic conductivity for the non-impregnated and the impregnated sample of HS shows lower permeabilities for the impregnated sample. The difference parallel to the lineation (x) is 1.5 µD at 5 MPa. With increasing pressure the difference decreases to 0.3 µD at 20 Mpa, while in the direction normal to the foliation (z) it is

0.8 µD at 5 MPa and 0.2 µD at 20 MPa. For the other samples (SZ, LS), the permeability/hydraulic conductivity is generally lower (see Table 1). Furthermore, only in the z-direction is the permeability of the non-impregnated samples greater than that of the impregnated samples. The inverted difference in the x-direction could possibly be caused by larger crystals of feldspar within the cylindrical specimen. This would also affect the preferred orientation of microcracks, which may serve as pathways for the flow medium.
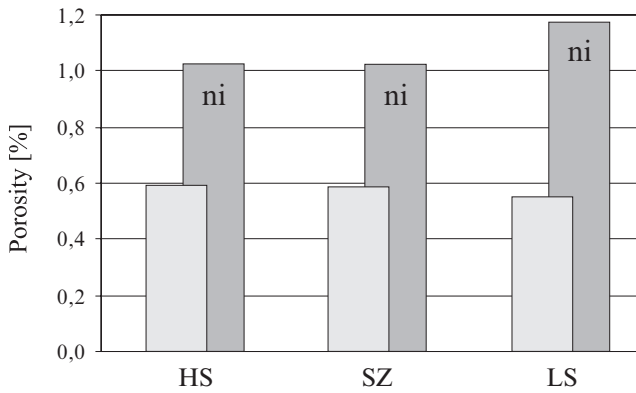
Figure 7. Porosity of the impregnated and non-impregnated (ni) samples.

Seismic velocities

A typical experimental data set for V_P as a function of pressure at room temperature is shown in Fig. 9. The P-wave velocities at atmospheric pressures are higher in saturated rocks than in those under dry conditions, owing to the limited compressibility of water-saturated pores and microcracks compared with air-filled ones (Figs 10 and 11). At higher confining pressures the curves are only slightly different (see Nur & Simmons 1969; Popp 1994). The influence of saturation depends on the matrix porosity. The results show that the V_P values at atmospheric pressure significantly increase for saturated samples. For impregnated rocks the V_P may be higher due to the higher Young's modulus of the acrylic resin compared with water (see Figs 10d, e and 11d, e).

At low confining pressure, the samples show a pronounced directional dependence (Figs 10a and 11a). $V_{P\min}$ can be observed normal to the foliation (3.22 km s^{-1}), whereas $V_{P\max}$ is parallel to the lineation (4.85 km s^{-1}) for SZ$_{\text{ni}}$. This sample also shows a remarkable pressure dependence. The velocities of elastic waves increase with confining pressure, a fact which is usually attributed to progressive microcrack closure (see Figs 10b and 11b). The maximum pressure-dependent increase of V_P can be observed for the z-direction. In order to explain the low-pressure phenomena, ΔV_P (given by the difference between V_P values measured at 100 and at 3 MPa) was calculated for SZ$_{\text{ni}}$

(Fig. 11c). As mentioned above, the corresponding microcrack pattern is dominated by cleavage cracks in muscovite and biotite and phase boundary cracks.

For water-saturated conditions, the most pronounced increase in V_P as compared with dry conditions is observed subparallel to the foliation pole, and this can be related to the saturation of grain boundary cracks. This is clearly demonstrated in the ΔV_P stereogram (Fig. 11f), where the difference is given for saturated and dry conditions. For the non-impregnated sample, the maximum V_P velocities are 4.70 km s^{-1} (dry) and 5.56 km s^{-1} (sat), while 5.14 km s^{-1} (dry) and 5.66 km s^{-1} (sat) were measured for the impregnated samples. Both samples (impregnated and non-impregnated) show comparable velocity distributions (Figs 10d to f and 11d to f). The velocity patterns agree with those obtained from the non-impregnated samples. However, the impregnated sample shows a significantly higher velocity especially within the foliation normal, while the high-velocity direction is less affected (Figs 10d to f). Comparing Fig. 10(f) and Fig. 11(f), it becomes evident that the observed microcrack population was sealed with acrylic resin. The grain boundary cracks, which are mainly orientated parallel to the foliation, reflect the open connected porosity at *in situ* conditions.

The anisotropy of V_P, expressed as $[(V_{P\max} - V_{P\min})/V_{P\max}] \times 100$, amounts to 21.8 per cent (SZ), 10.3 per cent (LS) and 17.0 per cent (HS), and reflects the stronger fabric anisotropy of the shear-zone sample when compared to the other samples.

DISCUSSION

Microcrack fabric and texture

All samples show many different types of open *in situ* micro-cracks which can be optically discriminated by the injection of the fluorescent acrylic resin. For non-impregnated open cracks, however, it is still unclear whether they existed *in situ* but were not interconnected with the crack network, or whether they formed during core relaxation or later sample treatment. Microstructural features which are unequivocally indicative of an artificial crack origin, such as open crack segments in the prolongation of impregnated cracks, were not observed. It was possible to identify distinct sets of microcracks forming patterns which strongly depend on the size and shape parameters and textures of their host minerals. For this reason, the geometry of
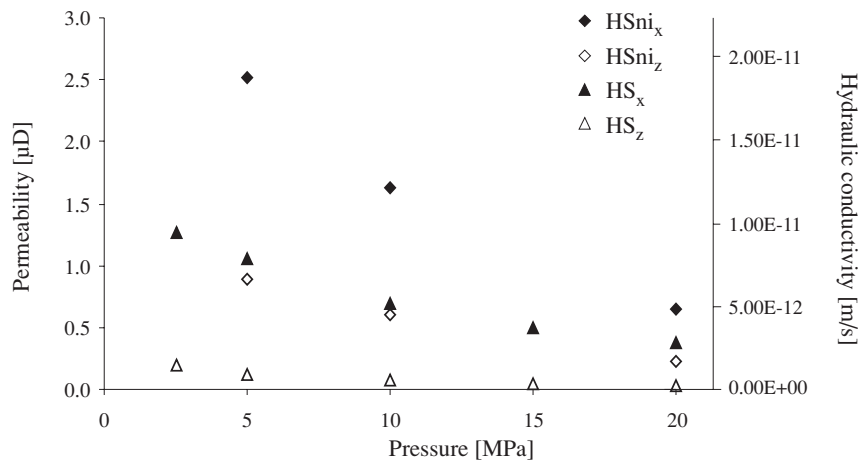

Figure 8. Pressure-dependent permeability/hydraulic conductivity of sample HS, impregnated and non-impregnated (ni) in the x- and z-directions.
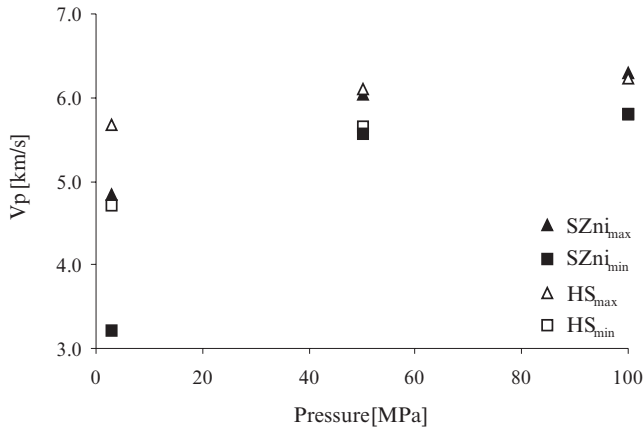
Figure 9. Pressure-dependent seismic velocity of the non-impregnated sample SZ and the impregnated sample HS for two selected propagation directions.

the crack patterns is closely related to the bulk rock fabrics; that is, it varies significantly from the shear zone into the less deformed wall rocks. The relative frequency and orientation of the various microcrack sets are schematically illustrated for each sample in Fig. 12, which is based on the intensity and the position of maxima in the corresponding crack pole figures (Fig. 6). Because of the weak preferred orientation of the intragranular cracks in quartz and intergranular cracks in quartz polycrystals, only the cracks in feldspars and micas could be represented in this way.

From direct observation of thin sections, it is obvious that in all samples the open *in situ* microcracks and intersections of different types build an interconnected network. The cleavage cracks, in particular, represent favoured planar pathways because of their smooth surface, while rough crack surfaces induce a lower hydraulic aperture. A second subordinate flow direction may be given by intersection lines between prominent crack sets.
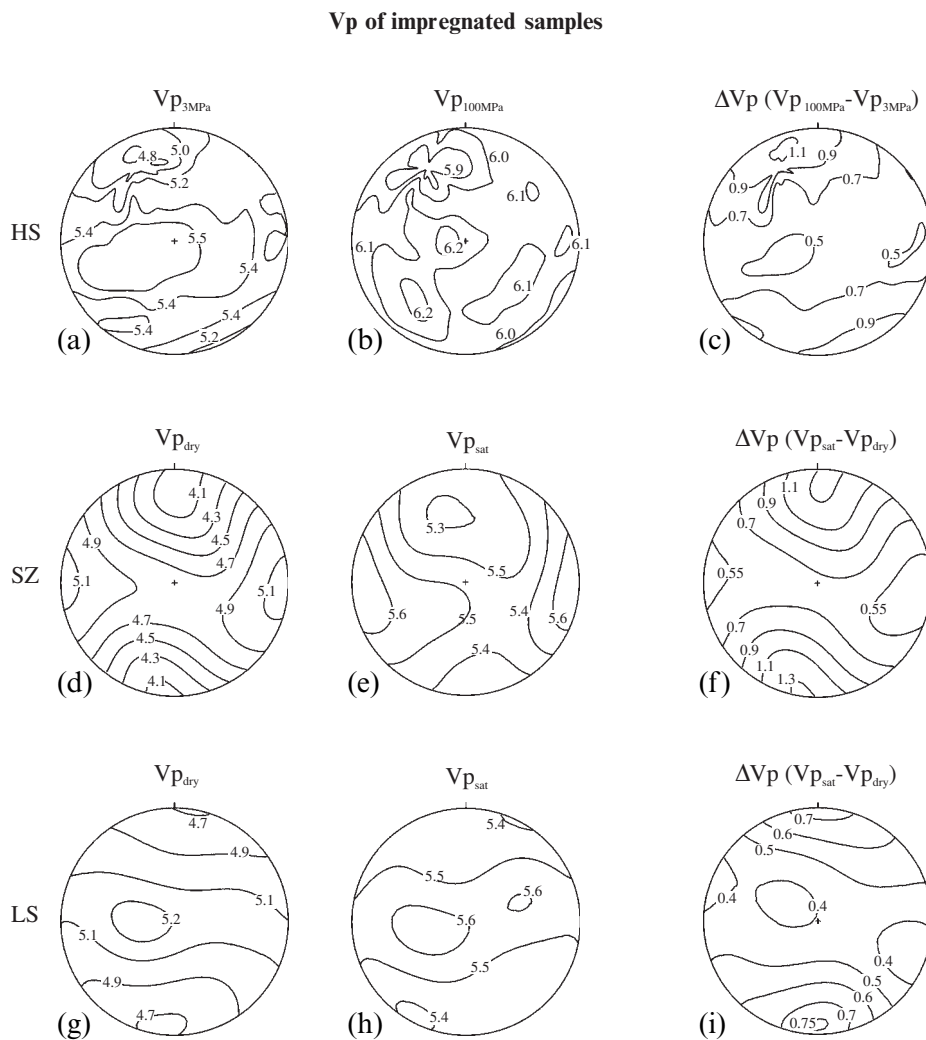
Vp of impregnated samples

Figure 10. Experimentally determined directional dependence of compressional wave velocities [km s^{-1}] for the impregnated samples HS, SZ and LS. (a) and (b) V_P as a function of confining pressure; (c) $\Delta V_{P(100-3\ \text{MPa})}$ between 100 and 3 MPa confining pressure; (d) and (g) V_P under dry conditions; (e) and (h) V_P under saturated conditions; and (f) and (i) $\Delta V_{P(\text{sat-dry})}$ as a measure of the microcrack-induced anisotropy; Schmidt net, lower hemisphere.
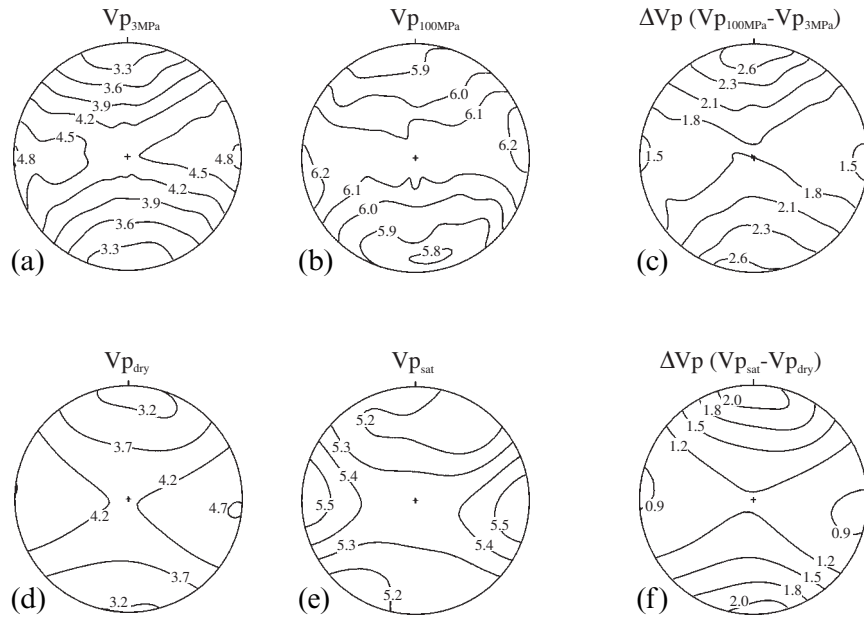
Vp of the non-impregnated sample SZ

Figure 11. Seismic velocity [km s^{-1}] of the non-impregnated sample SZ: (a) at a confining pressure of 3 MPa; (b) at a confining pressure of 100 MPa; (c) $\Delta V_{P(100-3 \text{ MPa})}$ between 100 and 3 MPa confining pressure; (d) V_P under dry conditions; (e) V_P under saturated conditions; and (f) $\Delta V_{P(\text{sat-dry})}$ as a measure of the microcrack-induced anisotropy; Schmidt net, lower hemisphere.

As mentioned above, the preferred orientation of the (001)-cleavage cracks of the micas is an indicator for the foliation strength. It is most clearly developed in the sample of the immediate shear zone (SZ) and the sample of the footwall (LS).

Porosity

In crystalline rocks, porosity determined in the laboratory yields consistent results, irrespective of the analytical method that is applied (e.g. Rasilainen *et al.* 1996). However, all laboratory methods suffer from the same systematic errors, namely the unquantified effects of stress relaxation, sampling procedures and sample preparation methods on the results.

Bossart & Mazurek (1991) used Hg-injection and water-loss measurements to measure the porosity of Grimsel granodiorite in the laboratory, and the values fall typically in the range 0.8–1.2 vol per cent. These values are relatively high for crystalline rocks that were not subjected to hydrothermal alteration. However, they can be explained by the abundance of microcrack systems and the substantial albitization of magmatic plagioclase during greenschist-stage metamorphism. These values are consistent with the data presented in Fig. 7 for samples that were not impregnated *in situ*.

Samples that were resin-impregnated *in situ* should result in zero porosity in the laboratory. However, as Fig. 7 shows, this is not the case, and values of about 0.6 vol per cent are measured. This porosity is probably artificial; that is, created by unloading and sample treatment. Thus *in situ* matrix porosity, calculated as the difference between the values for impregnated and non-impregnated samples, is about 0.4–0.5 vol per cent, which is one-third to one-half of the porosity that is measured on conventional samples in the laboratory. Thus either the pore

apertures in the natural microcrack system were enhanced, or new cracks were created due to unloading and sample treatment.

As discussed above, the design of the Connected Porosity experiment avoids a number of possible artefacts that affect porosity measurements in the rock matrix. Whereas the experiment represents a major step towards the characterization of *in situ* porosity, one uncertainty remains in that possible crack formation and related effects of porosity and pore connectivity by drilling the injection boreholes are as yet unquantified. Presently, there are no rigorous arguments that could quantify these effects. However, the similarity of matrix permeability derived from a large-scale ventilation test that characterizes the matrix well beyond the zone affected by the existence of the tunnel (see below) and the small-scale measurements presented here is a semi-quantitative argument that the possible crack formation during drilling of the injection boreholes does not have a substantial effect on matrix porosity and network structure.

Hydraulic conductivity/permeability

In order to estimate the *in situ* permeability/hydraulic conductivity, it is necessary to consider the *in situ* stress field. The maximum horizontal stress (σ_H) ranges between 18 and 45 MPa, and the minimum horizontal stress (σ_h) is almost 10 MPa less (Keusen *et al.* 1989). The lithostatic stress (σ_V) reaches 8 to 12 MPa, and the hydrostatic pressure (P) is 4 MPa. For average values, the effective stresses ($\sigma_{\text{eff}} = \sigma - P$) are estimated to be $\sigma_{\text{Heff}} = 30$ MPa, $\sigma_{\text{heff}} = 19$ MPa and $\sigma_{\text{Veff}} = 7$ Mpa. Hence the measurements at a confining pressure of 20 MPa and 30 MPa would give the best approximation of *in situ* conditions. This
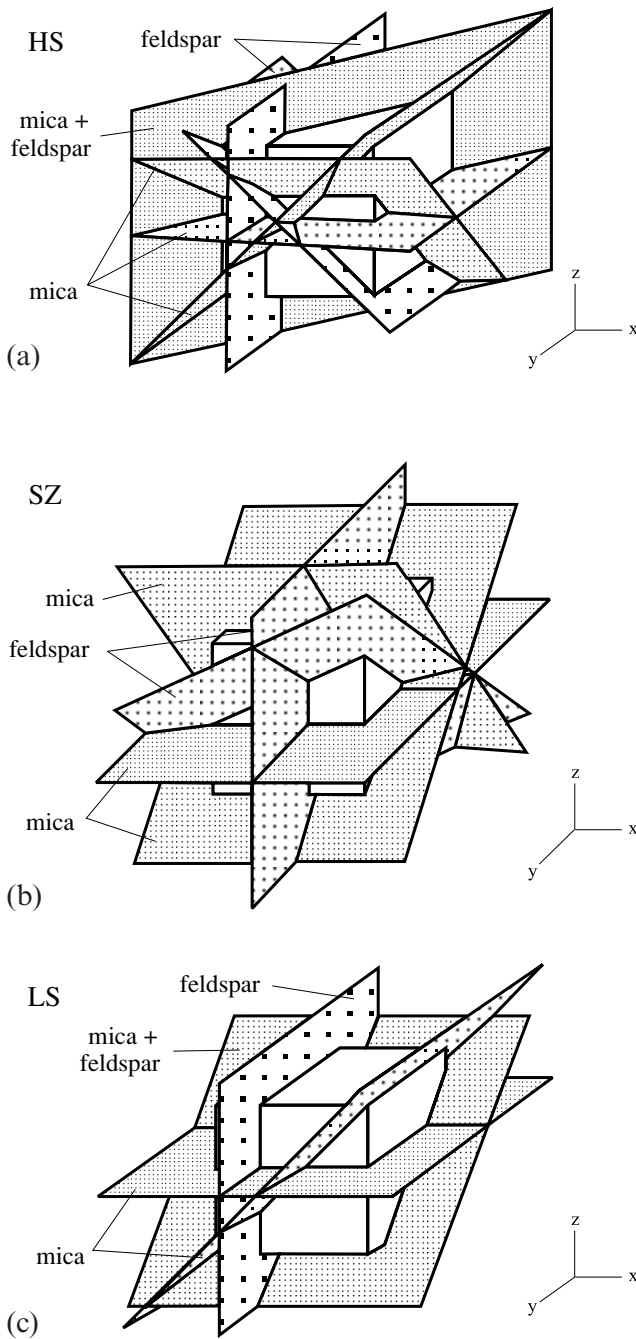
conductivity of impregnated samples is less than half the value of non-impregnated samples. The measured values are of the order of 10^{-11} m s^{-1}. Kull *et al.* (1993) derived large-scale (dekameters along tunnel) matrix conductivities by measuring the evaporative water discharge from the unfractured tunnel surface, with typical values of $1-3 \times 10^{-11}$ m s^{-1}. Thus the large-scale *in situ* measurements are quite consistent with the small-scale laboratory values presented here. It appears that unloading/sample preparation does not critically affect laboratory measurements. Therefore, the application of confining pressure for laboratory tests yields hydraulic conductivities similar to those measured *in situ*.

Seismic velocities

The rapid increase of V_P at low pressures up to 100 MPa as shown in Fig. 9 is associated with the progressive closure of microcracks (e.g. Birch 1961a,b; Brace 1965). At higher pressures the curves become nearly linear, indicating that intrinsic velocities are approached, reflecting the properties of a nearly crack-free rock volume. The assumption of isotropy is valid only for rocks with a random distribution of minerals, microcracks, pores, etc.—a very special case generally not fully realized in natural rocks. Most rocks are anisotropic when considering physical rock parameters as well as fabrics. Intrinsic elastic properties and anisotropy at higher pressures originate from the elastic properties of the constituent minerals and their crystallographic texture. The difference in velocities measured at high and low (below the crack-closing pressure) confining pressures should be mainly attributed to the contribution of microcracks or pores. Therefore, the spatial dependence of V_P has been studied exclusively on spherical samples, allowing the determination in any direction.

The pressure dependence of the complete V_P distribution and the observed dominant crack populations show a close relationship regarding the seismic anisotropy at low confining pressures. The most important observation is that, for saturated samples, the symmetry of the V_P distribution does not change with pressure in the impregnated nor in the non-impregnated samples. At high pressures, for which most of the cracks are closed, the residual anisotropy is mainly controlled by the texture of biotite and muscovite. The significance and effective influence of the bulk microcrack fabrics on V_P can be best demonstrated by the ΔV_P patterns. This is clearly indicated by the good correlation between crack pole figures and the corresponding V_P stereograms (compare Figs 6 and 10). Therefore, the influence of the preferred orientations of biotite and muscovite is twofold: they control the intrinsic properties and the orientation of the most significant microcracks, namely open microcracks parallel to the (001)-cleavage planes. Moreover, from comparison of the V_P characteristics of impregnated and non-impregnated samples and their saturation behaviour, it follows that the open *in situ* cracks are mostly interconnected.

To quantify the influence of the open *in situ* cracks on the V_P pattern, $\Delta V_{Pdry}(SZ_{imp} - SZ_{ni})$ as the difference between V_PSZ_{imp}(dry) and V_PSZ_{ni}(dry) has to be calculated. In this case, the residual ΔV_P pattern only reflects the contributions of sealed cracks (decorated with the acrylic resin) because the effects of the intrinsic properties, isolated open cracks and cracks originated by stress release after core extraction as well as sample treatment are eliminated (Fig. 13). The ΔV_P diagram
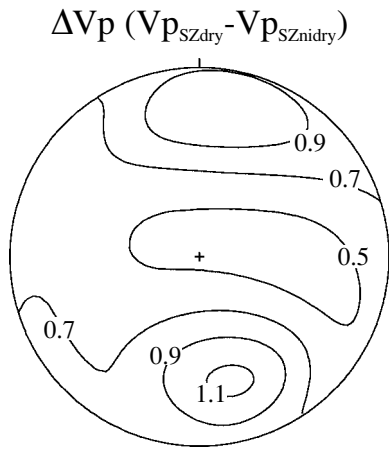

Figure 12. Schematic illustrations of microcrack orientation (dotted planes) in sample cubes for HS, SZ and LS with reference axes (*x*, *y*, *z*); the density of dots corresponds to the relative frequency of the various crack sets.

is only applicable for the non-impregnated samples, because for the impregnated samples only the artificial component was measured. The measured hydraulic conductivity at a confining pressure of 20 MPa ranges between 4.9×10^{-12} in the *x*-direction and 1.7×10^{-12} m s^{-1} in the *z*-direction for the non-impregnated sample HS. For SZ$_{ni}$ the hydraulic conductivity is 1.1×10^{-12} and 7.1×10^{-13} m s^{-1}, and for LS$_{ni}$ it is 5.6×10^{-13} and 1.0×10^{-12} m s^{-1}.

The dependence of hydraulic conductivity on confining pressure is relatively small. As shown in Fig. 8, the hydraulic

$$\Delta Vp\ (Vp_{SZdry}\text{-}Vp_{SZnidry})$$

Figure 13. Influence of the *in situ* microcracks on the directional dependence of V_P [km s^{-1}], represented as the difference of V_P between the impregnated and non-impregnated sample SZ under saturated conditions, $\Delta V_P = V_P SZ_{imp} - V_P SZ_{ni}$; Schmidt net, lower hemisphere; for further explanation see text.

indicates that, besides the cracks in mica, connected cracks in quartz and especially in feldspar contribute significantly. However, this observation is only valid if the core relaxation after impregnation and extraction is comparable for the samples SZ_{imp} and SZ_{ni} because the velocity difference between dry and saturated impregnated rock samples (Figs 10d, e and 11d, e) indicates a distinct amount of microcrack opening. In total, the *in situ* open microcracks are responsible for a porosity of about 0.5 per cent, given as the difference between $V_P SZ_{imp}$ and $V_P SZ_{ni}$.

CONCLUSIONS

The present study demonstrates that, by combining microfabric analyses, petrophysical investigations and *in situ* field observations, a quantitative evaluation of the crack-related rock properties is obtained, which represents a step towards a realistic representation of *in situ* matrix properties.

Detailed microfabric analysis clearly shows that several sets of open cracks form a complex bulk crack pattern. The orientation and relative frequency of individual sets of cracks strongly depend on the fabrics and textures of the related host minerals since cleavage cracks and intergranular cracks (grain and phase boundary cracks) predominate. The most significant fabric change from the wall rocks towards the centre of the shear zone is an increase of the intensity of the planar fabric which is best reflected by the orientation pattern of the (001)-cleavage planes. It can be assumed that the connectivity of the corresponding cleavage and intergranular cracks increases in the same direction. As a consequence, hydraulic conductivity and diffusivity in the mylonitic shear zone are minimal normal to the cleavage direction. An open question is, however, why the permeability in the shear zone (sample SZ) is lower than that in the wall rock (HS, LS).

Microstructural features that would enable a distinction to be made between isolated (non-impregnated) open *in situ* cracks and cracks formed during core relaxation and sample treatment were not observed. Therefore, a statistical comparison between impregnated and non-impregnated samples considering crack dimensions and crack frequencies would be a suitable approach.

From a comparison of the matrix porosity values obtained by standard laboratory techniques with the *in situ* values derived here we find that stress release and sample preparation in the laboratory enhance the obtained values by a factor of 2–2.5. A remaining unknown is the unquantified effect of drilling of the injection boreholes, such that the real *in situ* values could be even smaller. Similar conclusions are drawn for matrix permeability. Assuming a confining pressure of 20 Mpa, which closely approximates the *in situ* conditions, a hydraulic conductivity between 7.1×10^{-13} and 10^{-12} m s^{-1} was evaluated as a realistic value. The anisotropy of the permeability/hydraulic conductivity is strongly related to the rock foliation. Usually, the corresponding values are smallest normal to the foliation. From microcrack data it is obvious that mainly (001)-cleavage cracks in mica and cracks in feldspars as well as cracks in quartz and their interconnectivities also control the directional dependence of the hydraulic properties at higher confining pressures.

As a whole, the V_P data reflect the composite microcrack fabric, especially the preferred orientation of the mica cleavage cracks and the grain/phase boundary cracks. A strong geometric relationship between the ΔV_P stereograms and the crack pole figures regarding the impregnated and non-impregnated samples under dry and water-saturated conditions and higher confining pressures indicates that the multidirectional V_P anisotropy is mainly caused by the observed and quantified crack fabrics. In fact, the ΔV_P values between impregnated and non-impregnated samples reflect the bulk microcrack patterns which effectively influence the V_P anisotropy at lower confining pressure (below 20 MPa). An influence especially of the cracks in mica, connected cracks in quartz and those in feldspar could also be recognized in the ΔV_P stereogram. These sets of cracks, which are mainly orientated parallel to the foliation, also produce a marked open connected porosity under *in situ* conditions at the Grimsel Test Site. Moreover, the direct comparison of V_P under dry and saturated conditions allows a quantitative measure between open *in situ* cracks and effects that originate either from stress release after core extraction or sample treatment.

The fact that the microporous matrix was impregnated by resin under *in situ* conditions means that an interconnected system of microcracks exists and is accessible to fluids. This conclusion is corroborated by microscopic fabric analysis and ancillary petrophysical measurements. Even though the *in situ* matrix porosity is less than half of the porosity measured on unloaded samples in the laboratory, it represents the dominant fluid reservoir of the formation, containing substantially more water than fractures on a large scale.

These conclusions have a practical aspect in that the efficiency of matrix diffusion as a retardation process for contaminant transport through fractured media may be somewhat smaller than expected on the basis of laboratory measurements of porosity on stress-released samples. On the other hand, and maybe more importantly, this study indicates that interconnected networks of microcracks occur throughout the entire rock volume and are not restricted to the immediate surroundings of macroscopic fractures in which flow and transport occur.

In short-term migration experiments that have previously been conducted at the Grimsel Test Site, it has only been possible to demonstrate the existence of matrix diffusion from macroscopic brittle faults into highly porous fault gouges (Heer & Smith 1998); the experimental timescales (days to months) were too short to positively identify diffusion into the rock matrix unaffected by major brittle deformation.

REFERENCES

Anderson, D.L., Minster, B. & Cole, D., 1974. The effect of oriented cracks on seismic velocities, *J. geophys. Res.,* **79,** 4011–4015.

Birch, F., 1961a. The velocity of compressionel waves in rocks to 10 kilobars; Part 1, *J. geophys. Res.,* **65,** 1083–1102.

Birch, F., 1961b. The velocity of compressionel waves in rocks to 10 kilobars; Part 2, *J. geophys. Res.,* **66,** 2199–2224.

Bossart, P. & Mazurek, M., 1991. Structural geology and water flow-paths in the Migration shear-zone, *Nagra Technical Report NTB 91–12,* Nagra, Wettingen, Switzerland.

Brace, W.F., 1965. Some new measurements of linear compressibility of rocks, *J. geophys. Res.,* **70,** 391–398.

Choukroune, P. & Gapais, D., 1983. Strain pattern in the Aar granite (Central Alps): Orthogneiss developed by bulk inhomogeneous flattening, *J. struct. Geol.,* **5,** 411–418.

Dempster, T.J., 1986. Isotope systematics in minerals: biotite rejuvenation and exchange during Alpine metamorphism, *Earth. planet. Sci. Lett.,* **78,** 355–367.

France-Lanord, C., Sheppard, S.M.F. & Le Fort, P., 1988. Hydrogen and oxygen isotope variations in the High Himalaya peraluminous Manaslu leucogranite: evidence for heterogenous sedimentary source, *Geochim. Cosmochim. Acta.,* **52,** 513–526.

Frieg, B., Alexander, W.R., Dollinger, H., Bühler, C., Haag, P., Möri, A. & Ota, K., 1998. In situ resin impregnation for investigating radionuclide retardation in fractured repository host rocks, *J. contam. Hydrol.,* **35,** 115–130.

Hallbauer, D.K., Wagner, H. & Cook, N.G.W., 1973. Some observations concerning microscopic and mechanical behaviour of quartzite specimen in stiff, triaxial compression tests, *Int. J. Rock. Mech. Min. Sci. Geomech. Abstr.,* **10,** 713–726.

Heer, W. & Smith, P.A., 1998. Modelling the radionuclide migration experiment at Grimsel. What have we learned? *Mat. Res. Soc. Symp. Proc.,* **506,** 663–670.

Hellmuth, K.H., Klobes, P., Meyer, K., Röhl-Kuhn, B., Siitari-Kauppi, M., Hartikainen, J. & Timonen, J., 1995. Matrix retardation studies: size and structure of the accessible pore space in fresh and altered crystalline rock, *Z. geol. Wiss.,* **23,** 691–7066.

Keusen, H.R., Ganguin, J., Schuler, P. & Buletti, M., 1989. Felslabor Grimsel: Geologie, *Nagra Technical Report NTB 87–14,* Nagra, Wettingen, Switzerland.

Kowallis, B.J. & Wang, H.F., 1983. Microcrack study of granitic cores from Illinois deep borehole UPH-3, *J. geophys. Res.,* **88,** 7373–7380.

Kull, H., Brewitz, W. & Klarr, K., 1993. Felslabor Grimsel—Ventilationstest, In situ-Verfahren zur Permeabilitätsbestimmung im Kristallin, *Nagra Technical Report NTB 91–02,* Nagra, Wettingen, Switzerland.

Marquer, D. & Gapais, D., 1985. Les massifs cristallins externes sur une transversale Guttannen—Val Bedretto (Alpes Centrales): structures et histoire cinématique, *C. R. Acad. Sci. Paris,* **301/II,** 543–546.

Marquer, D., Gapais, D. & Capdevita, R., 1985. Comportement chimique et orthogneissification d'une granodiorite en faciès schistes verts (Massif de l'Aar, Alpes Centrales), *Bull. Minéral.,* **108,** 209–221.

Mazurek, M., 2000. Geological and hydraulic properties of water-conducting features in crystalline rocks, in *Hydrogeology of Crystalline Rocks,* pp. 2–3, eds Stober, I. & Bucher, K., Kluwer Scientific Publishers, Dordrecht.

Möri, A., Adler, M. & Bühler, C., 1999. Connected Porosity (CP)—Feasibility studies and in situ resin injection experiment, *Nagra Internal Report,* Nagra, Wettingen, Switzerland.

Möri, A., Bühler, C., Haag, P. & Ota, K., 1996. Connected Porosity (CP)—Visualising the pore space in crystalline rock matrix using fluorescent acrylic resin, *Nagra Internal Report,* Nagra, Wettingen, Switzerland.

Neretnieks, I., 1980. Diffusion in the rock matrix: An important factor in radionuclide retardation? *J. geophys. Res.,* **85,** 4379–4397.

Norton, D. & Knapp, R., 1977. The nature of porosity, *Am. J. Sci.,* **277,** 913–936.

Nover, G., Heikamp, S., Kotny, A. & Duba, A., 1995. The effect of pressure on the electrical conductivity of KTB rocks, *Surv. Geophys.,* **16,** 63–81.

Nur, A. & Simmons, G., 1969. The effect of saturation on velocity in low porosity rocks, *Earth. planet. Sci. Lett.,* **7,** 183–193.

Peng, S. & Johnson, A.M., 1972. Crack growth and faulting in cylindrical specimen of Chelmsford granite, *Int. J. Rock. Mech. Min. Sci.,* **9,** 37–86.

Popp, T., 1994. Der Einfluss von Gesteinsmatrix, Mikrogefügen und Intergranularen Fluiden auf die elastischen Wellengeschwindigkeiten und die elektrische Leitfähigkeit krustenrelevanter Gesteine unter PT-Bedingungen, *PhD thesis,* University of Kiel, Kiel.

Rasilainen, K., Hellmuth, K.H., Kivekäs, L., Melamed, A., Ruskeeniemi, T., Siitari-Kauppi, M., Timonen, J. & Valkiainen, M., 1996. An interlaboratory comparison of methods for measuring rock matrix porosity, *VTT Research Notes 1776,* Technical Research Centre of Finland, Espoo, Finland.

Schild, M., 1999. Verbundene Mikroporositäten in Kristallingesteinen-Fallstudie Felslabor Grimsel, *PhD thesis,* University of Göttingen, Göttingen.

Siegesmund, S., Vollbrecht, A., Chlupac, T., Nover, G., Dürrast, H., Müller, J. & Weber, K., 1993. Fabric-controlled anisotropy of petrophysical properties observed in KTB core samples, *Sci. Drill.,* **4,** 31–54.

Siitari-Kauppi, M., Flitsiyan, E.S., Klobes, P., Meyer, K. & Hellmuth, K.H., 1998. Progress in physical rock matrix characterization: Structure of the pore space, *Mat. Res. Soc. Symp Proc.,* **506,** 671–678.

Steck, A., 1968. Die alpidischen Strukturen in den Zentralen Aaregraniten des westlichen Aarmassivs, *Eclog. Geol. Helv.,* **61,** 19–48.

Vollbrecht, A., Rust, S. & Weber, K., 1991. Development of microcracks in granites during cooling and uplift: examples from the Variscan basement in NE Bavaria (FRG), *J. struct. Geol.,* **7,** 787–799.

Vollbrecht, A., Dürrast, H., Kraus, J. & Weber, K., 1994. Paleostress directions deduced from microcrack fabrics in KTB core samples and granites from the surrounding area, *Sci. Drill.,* **4,** 233–241.